Available online at www.sciencedirect.com
ScienceDirect
Journal of the European Ceramic Society 31 (2011) 199–215
www.elsevier.com/locate/jeurceramsoc

Oxidation behavior of hot pressed ZrB_2–SiC and HfB_2–SiC composites

Manab Mallik, K.K. Ray, R. Mitra *

Department of Metallurgical and Materials Engineering, Indian Institute of Technology, Kharagpur 721302, West Bengal, India

Received 1 March 2010; received in revised form 9 August 2010; accepted 25 August 2010
Available online 21 September 2010

Abstract

Non-isothermal, isothermal and cyclic oxidation behavior of hot pressed ZrB_2–20 (vol.%) SiC (ZS) and HfB_2–20 SiC (HS) composites have been compared. Studies involving heating in thermogravimetric analyzer have shown sharp mass increases at 740 and 1180 °C for ZS, and mass gain till 1100 °C followed by loss for HS. Isothermal oxidation tests for 1, 24 and 100 h durations at 1200 or 1300 °C have shown formation of partially and completely stable oxide scales after ~24 h exposure for ZS and HS, respectively. X-ray diffraction, scanning electron microscopy and energy or wavelength dispersive spectroscopy has confirmed presence of ZrO_2 or HfO_2 in oxide scales of ZS or HS, respectively, besides B_2O_3–SiO_2. Degradation appears more severe in isothermally oxidized ZS due to phase transformations in ZrO_2; and is worse in HS on cyclic oxidation at 1300 °C with air cooling, because of higher thermal residual stresses in its oxide scale.

Keywords: B. Composites; C. Residual stress; C. Hardness; D. Borides; Oxidation

1. Introduction

Ultra-high temperature ceramics (UHTCs) based on ZrB_2 and HfB_2 are a class of materials with melting temperatures exceeding 3000 °C, high physical stability (due to absence of phase transformations) and thermal conductivity as well as ability to retain strength at elevated temperatures. Earlier studies[1,2] on isothermal oxidation of ZrB_2 between 800 and 1100 °C have shown formation of ZrO_2 and an outer protective layer of B_2O_3 (l), which restricts the inward diffusion of oxygen anions. However, at temperatures ≥1100 °C, the vapor pressure of B_2O_3 is increased sharply,[2,3] leading to its vaporization with simultaneous acceleration in the oxidation rates of ZrB_2 and HfB_2. As both ZrO_2 and HfO_2 are anion deficient semiconductors with oxygen vacancies, the diffusion of oxygen anions has been found to be significant in these oxides. Hence, ZrB_2 and HfB_2 in their monolithic form are not suitable for ultra-high temperature applications in aero-propulsion systems due to their poor oxidation resistance.[4,5] Reinforcement of these UHTCs with either SiC or $MoSi_2$ improves both oxidation resistance and mechanical properties of these materials significantly, as has been reported in some of the earlier studies.[6,7] Earlier reports[8,9] have shown that the presence of 20 vol.% SiC is the requirement for achieving optimum properties in the ZrB_2 based composites. In fact, it has been shown[9–11] that ZrB_2–SiC and HfB_2–SiC composites are attractive for potential applications in extreme thermal environments like that associated with hypersonic flight, atmospheric re-entry, and rocket propulsion. Moreover, Loehman[12] has proposed that the most promising material for use in sharp leading edges on hypersonic vehicles are the composites of these ceramics with SiC reinforcements.

The presence of SiC reinforcements in ZrB_2 and HfB_2 based ceramic composites leads to reduction in their rates of oxidation by formation of a protective scale of glassy B_2O_3–SiO_2, which is more viscous and stable, as well as less volatile than B_2O_3 alone.[3,4,7,13–17] This amorphous silica-rich scale has low diffusivity for oxygen due to its high viscosity, and has been found to be protective till at least 1600 °C in oxidizing environments.[6,18,19] An added advantage is its sufficient fluidity to fill up the pores or discontinuities present in the skeleton of ZrO_2 or HfO_2, and thus fully cover the sample surfaces due to its excellent wettability.[20–23] Diffusion of dissolved oxygen through semi-solid B_2O_3–SiO_2 present in the capillaries within porous ZrO_2 or HfO_2 and at the base of oxidation products has been proposed as the rate limiting step for oxidation up to 1400 °C.[23] For the HfB_2–SiC composites,[6] release of volatile products has been found to have a significant role till 1350 °C,

* Corresponding author. Tel.: +91 3222 283292; fax: +91 3222 282280.
E-mail address: rahul@metal.iitkgp.ernet.in (R. Mitra).

0955-2219/$ – see front matter © 2010 Elsevier Ltd. All rights reserved.
doi:10.1016/j.jeurceramsoc.2010.08.018

while presence of SiC reinforcements has been reported as beneficial at temperatures ≥1400 °C.

The oxidation resistance of ZrB_2 has been reported as inferior to that of HfB_2 due to volume changes during phase transformations in ZrO_2 and lower oxygen diffusivity in HfO_2.[22] However, it should be noted that the published reports are not exhaustive for intermediate temperature domain (≤1400 °C), and variation in experimental conditions could yield quite different results, which justifies the requirement for further studies emphasizing specific aerospace engineering applications. As oxidation kinetics and stability of oxide scale are known to be strongly dependent on both time of exposure and thermal shock, many high temperature engineering applications require further studies to address these issues.

The present study is focused on a comparative assessment of non-isothermal, isothermal and cyclic oxidation behavior of ZrB_2–20 (vol.%) SiC (ZS) and HfB_2–20 SiC (HS) composites, prepared by hot pressing under identical conditions. A preliminary report on mechanical, thermal and oxidation properties of ZS has been published elsewhere.[24] The objectives and scope of the present study on ZS and HS include: (i) identification of the critical temperatures for oxidation during heating from the ambient to 1300 °C; (ii) assessment of mass change with time during isothermal exposure for either 24 or 100 h at 1200 and 1300 °C in air; (iii) comparison of mass changes in course of cyclic oxidation at 1300 °C with that during isothermal tests at the same temperature; (iv) analysis of oxide scale constituents; (v) measurement of residual stresses in the oxide scale; (v) comparison of the mechanisms of oxidation under different test conditions for each composite; and (vi) comparison of damage due to combined effects of oxidation and thermal shock.

2. Experimental procedure

2.1. Preparation and characterization of materials

The powders of ZrB_2 and SiC were obtained from H.C. Starck Ltd. (H.C. Starck GmbH, Im Schleeke, Goslar, Germany), while the HfB_2 powder was obtained from Johnson Maththey Inc., USA. The purity of all the as-received powders was ≥99.5%. The powders were weighed in suitable proportion, and then intimately mixed by milling using WC-Co vials and balls in a planetary mono-mill (Fritsch GmbH, Idar-Oberstein, Germany) operated at a speed of 250 rpm for 2 h. The powder mixtures were sintered under uniaxial pressure of 30 MPa using graphite dies lined with grafoil inside a resistance heating furnace operated at 2000 °C for 30 min in argon environment, to prepare pellets of 42 mm diameter and 4 mm thickness.

The densities of hot pressed composites were measured using Archimedes principle. For microstructural studies, the hot-pressed pellets were first sectioned with the help of an Isomet slow speed diamond saw (Buehler Ltd., Lake Bluff, IL, USA), and then sequentially polished using diamond coated discs, abrasive SiC papers, and clothes smeared with diamond lapping paste (0.25 μm). The different phases present in the microstructures were identified by X-ray diffraction (XRD) analysis. Thereafter, the microstructures of the samples were examined using secondary electron (SE) and backscattered electron (BSE) imaging modes on a field emission scanning electron microscope (FESEM, Zeiss Supra 40, Carl Zeiss NTS GmbH, Oberkochen, Germany), where chemical compositions of different phases were examined using energy dispersive spectroscopy (EDS). The data from about 100 measurements was averaged to obtain the average sizes of matrix grains or SiC particles, as mentioned above.

2.2. Oxidation tests

2.2.1. Non-isothermal oxidation tests

Small specimens of either ZS or HS, having dimensions of approximately 0.5 mm × 1.5 mm × 1.5 mm and mass ≈10 mg, were kept in alumina crucibles and then subjected to heating at the rate of 10 °C/min from 50 to 1300 °C in flowing air inside a thermogravimetric analyzer (TGA, Perkin-Elmer, Waltham, MA, USA). A mass of 10 mg was considered as optimum to have sufficient sensitivity and to avoid the presence of thermal gradient within the sample.[25] The change in mass of the specimens in course of heating was measured using dry alumina (Al_2O_3) powder as reference. These tests were carried out primarily to determine both the critical temperatures for oxidation, and the mass changes in course of heating, so as to get an idea about early stages of oxidation.

2.2.2. Isothermal oxidation tests

Isothermal oxidation tests were carried out on samples of both ZS and HS in dry air at temperatures of either 1200 or 1300 °C for both 24 and 100 h. Rectangular bars with dimensions of 10 mm × 4 mm × 4 mm were sliced from the hot-pressed pellets, and were mechanically polished up to 0.25 μm diamond finish for use as specimens for these tests. These specimens were wrapped using platinum wire, and then suspended by hooking to a 1.5 m long straight nichrome wire inside the vertical chamber of a SiC-resistance heating furnace, through a hole in the ceramic plug used to close the top opening. Both the inner wall of the furnace and ceramic plug were made of Al_2O_3 (80%)–SiO_2, and neither of these were in contact with the specimen. The nichrome wire was hung at its upper end from the weighing pan of a mechanical balance (KEROY Private Limited, Varanasi, India) with least count of 0.1 mg. The sample mass was recorded prior to and during oxidation at intervals of either 1 or 6 h for tests conducted up to 24 or 100 h, respectively. Further experiments were carried out for a period of 1 h at either 1200 or 1300 °C with measurements of mass at intervals of 10 min in order to examine the isothermal kinetics during early stages of oxidation. The specimen temperature was measured using Pt–Pt/Rh thermocouple. Some of the experiments were repeated to ensure reproducibility of the results. Moreover, the nichrome and platinum wires were separately exposed to 1300 °C, and the total change in mass after exposure for a period of 24 h was recorded using an electronic balance (Sartorius AG, Goettingen, Germany).

2.2.3. Cyclic oxidation tests

The experimental setup, as well as dimensions and method of preparation of specimen were same as that used for isother-

mal oxidation tests. For the tests, each sample was inserted within the furnace at 1300 °C, isothermally held there for an hour, withdrawn from the furnace, and air cooled to room temperature (RT = 27 °C). This cycle was repeated 24 times, and mass change was measured at the beginning and end of each cycle.

2.2.4. Characterization of oxide scales

The oxide scales formed on the samples subjected to both isothermal and cyclic exposures were examined by XRD analysis using Cu Kα X-ray radiation for identification of the constituent phases, and by FESEM and EDS examinations to study their microstructures and compositions, respectively. Subsequently, the oxidized samples were hot-mounted using an electrically conductive copper-resin powder mixture, and then metallographically polished for examination of the cross-sections using both FESEM with EDS and electron-probe microanalyzer (EPMA, CAMECA SX 100, 92622 Gennevilliers Cedex, France) with wavelength dispersive spectroscopy (WDS). The oxide scale thicknesses were averaged out of measurements from about 10 different locations. For detection of boron, the SEM was operated at acceleration voltage of 5 kV during part of the EDS analysis, following the procedure recommended in an earlier study.[26] However, it is considered difficult to detect boron by EDS analysis, and hence WDS attached to EPMA was used for this purpose.[27]

The biaxial residual stress in the selected phases of the oxide scales was measured by XRD analysis using the $\sin^2\psi$ technique.[28–30] In a given XRD pattern, the highest peak having no overlap with the neighboring peaks was specifically chosen for the residual stress measurement. The peaks of monoclinic ZrO_2 ($\bar{1}\,1\,1$) and HfO_2 ($\bar{1}\,1\,1$) were considered, taking into account the interplanar spacing (d_0) of the planes in the unstrained condition. A rocking technique involving tilting of the sample was used, and the d-spacing (d_ψ) was measured for different angles, ψ between the surface normal and the normal to the diffracting ($h\,k\,l$) plane. The biaxial stress was calculated from the slope of the best-fit lines for the plot of d_ψ against $\sin^2\psi$.

The amount of degradation beneath the oxide scale during the above-mentioned conditions of exposure at elevated temperature has been estimated by measuring the variation of microhardness from the scale/alloy interface to the center of the specimen. These tests were carried out using a diamond indenter fitted to a Vickers microhardness tester (Micromet 5103, Buehler Ltd., Lake Bluff, IL, USA), which was operated at a load of 500 g.

3. Results

3.1. Microstructure

The relative densities of ZS and HS found by Archemedes' principle are 99% and 96%, respectively. Fig. 1(a) and (b) shows the SEM (BSE) images depicting the microstructures of ZS and HS, respectively. These images reveal a uniform distribution of the constituent phases, with ZrB_2 or HfB_2 phases appearing brighter than SiC due to lower atomic number of the latter phase. Identification of the phases present in these images is based on qualitative confirmation of composition by EDS analysis. Close examination of microstructures of these composites in SEM has not shown much evidence of porosity. The matrix grain sizes of ZS and HS have been found as 5.94 ± 2.25 and 6.95 ± 3.04 μm, respectively, with the average SiC particle size being 5.77 ± 3.49 μm.

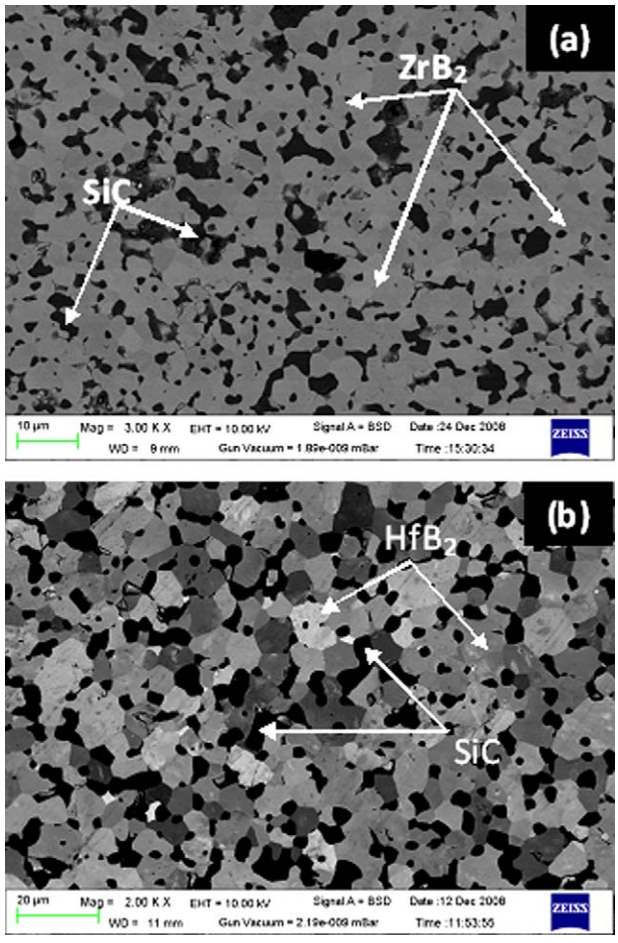

Fig. 1. SEM (BSE) images showing the microstructures of the investigated composites: (a) ZrB_2–20 vol.% SiC (ZS), and (b) HfB_2–20 vol.% SiC (HS). The constituent phases are shown with arrows.

3.2. Non-isothermal oxidation

Plots depicting the variation of mass change with respect to initial mass of ZS and HS with temperature, obtained from studies using TGA are shown in Fig. 2. The results in this figure indicate that mass gain starts at 740 °C for the ZS, continues at an approximately constant rate up to1200 °C, above which a relatively sharp increase in mass gain is observed. On the other hand, mass gain is initiated in HS at around ∼500 °C, is relatively small till 700 °C, and is increased almost linearly with temperature in the range of ∼700–1100 °C, followed by mass loss causing an apparent decrease in total mass increase. It should also be noted that the mass gain observed at a given temperature in HS is lower than that for ZS.

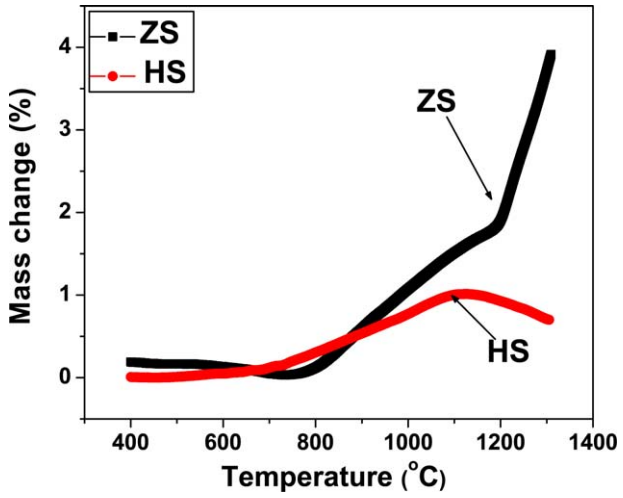

Fig. 2. Plots depicting the variation of mass change with temperature for ZS and HS, observed on heating in air inside TGA from room temperature to 1300 °C at the rate of 10 °C/min.

3.3. Isothermal and cyclic oxidation

3.3.1. Mass changes

Plots depicting the variation of mass change with time due to isothermal exposure of ZS and HS composites for 1, 24 and 100 h are shown in Figs. 3–5, respectively. Isothermal exposures of the nichrome and Pt wires at 1300 °C for 24 h have been found to show total mass changes of +0.189 mg/cm^2 (gain) and −0.006 mg/cm^2 (loss), respectively, which appear to be negligible compared to the mass changes observed for the ZS and HS on being subjected to similar tests (Fig. 4). The loss in mass observed for Pt resembles the results of an earlier study by Alcock.[31] The results depicted in Fig. 3 shows negative mass change (net mass loss) in HS at the 10th minute of exposure at 1200 °C and at both 20th and 30th minute of exposure at 1300 °C. In contrast, net mass gain has been observed on exposure of ZS at both 1200 and 1300 °C.

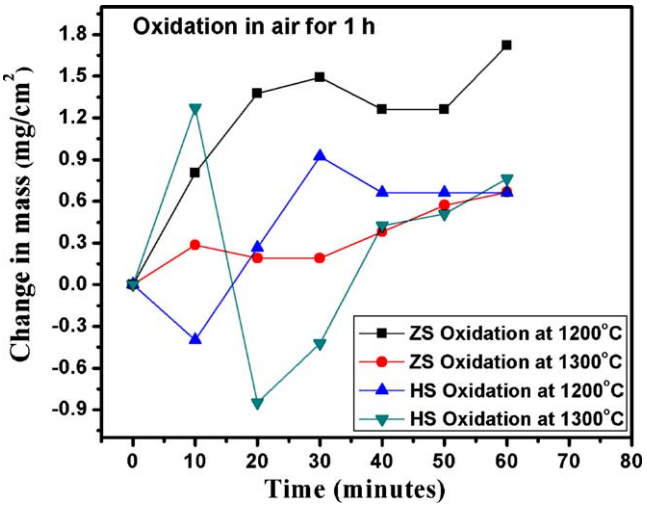

Fig. 3. Plots of change in mass against time, obtained for isothermal oxidation tests carried out on ZS and HS at 1200 and 1300 °C for duration of 1 h.

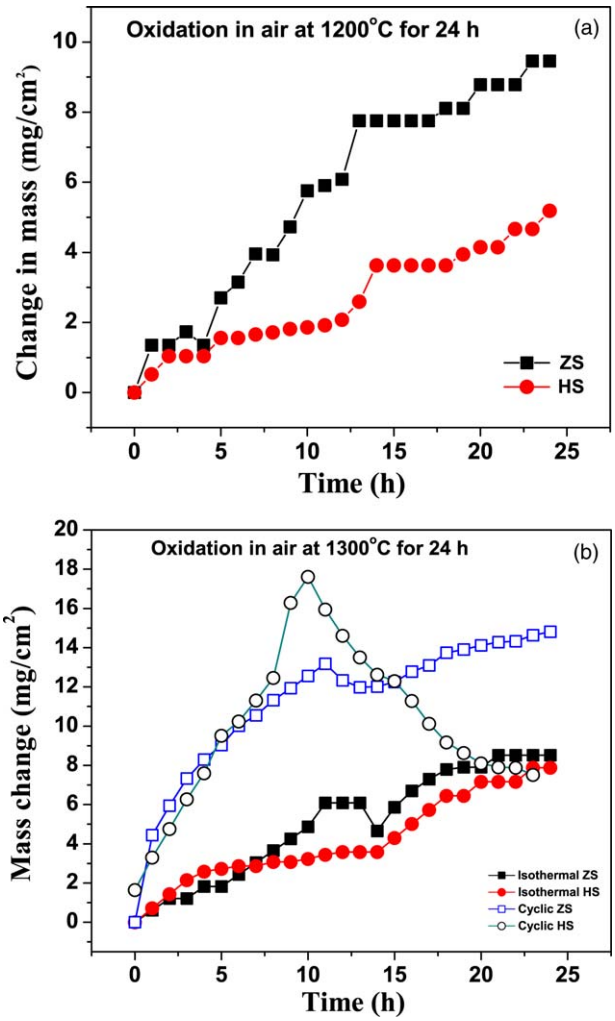

Fig. 4. Plots of change in mass against time, obtained from oxidation tests carried out on ZS and HS for duration of 24 h at: (a) 1200 °C under isothermal conditions, and (b) 1300 °C under both isothermal and cyclic conditions.

Examination of the nature of plots representing isothermal exposure for 24 h at either 1200 [Fig. 4(a)] or 1300 °C [Fig. 4(b)] indicates that mass gain takes place continuously for both the composites with short intervals, at which mass change is not apparent. The results of cyclic oxidations tests carried out at 1300 °C are also included in Fig. 4(b) for the purpose of comparison. Each data point on the curves for the cyclic oxidation behavior represents a single thermal cycle applied to the specimen. The plots depicting cyclic oxidation show that the HS undergoes a significant mass gain in the initial 10 cycles followed by sharp mass loss, while ZS shows almost similar mass gain as HS for up to 7 cycles, and then a reduced rate of increase in mass. Comparison of the results of cyclic and isothermal oxidation tests, as shown in Fig. 4(b) indicates that: (i) mass changes due to cyclic oxidation are higher for both the composites at a given time interval; (ii) mass appears to increase during isothermal oxidation in steps with brief intervals of no apparent mass change; and (iii) mass increases or decreases during cyclic exposures more or less continuously with no apparent regime of zero mass change (unlike that observed in course of isothermal exposure).

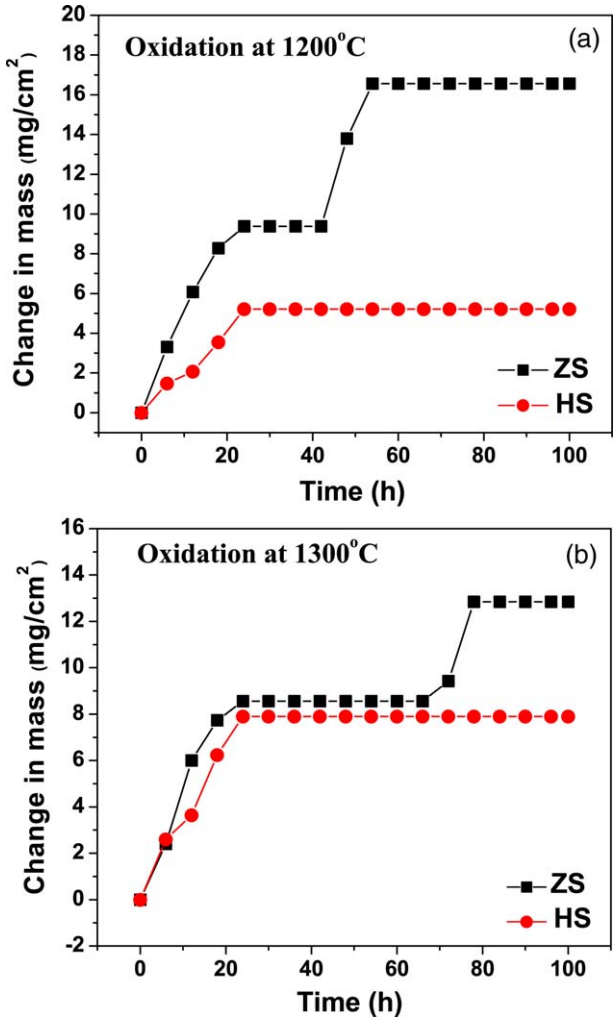

Fig. 5. Plots of change in mass against time, obtained from isothermal oxidation tests carried out in air on ZS and HS for duration of 100 h at: (a) 1200 °C, and (b) 1300 °C.

The results of studies involving isothermal exposure of HS for 100 h indicate the presence of a stable regime with no mass gain beyond 24 h at both 1200 [Fig. 5(a)] and 1300 °C [Fig. 5(b)]. On the other hand, ZS shows such stability only temporarily with abrupt mass gain after 40 and 65 h of exposure at 1200 [Fig. 5(a)] and 1300 °C [Fig. 5(b)], respectively. It should be noted that the net mass gain of the HS after 100 h at a given temperature is almost same as that after 24 h of exposure.

3.3.2. Oxide scales

3.3.2.1. Phase identification and morphology. The oxidation reactions and products for both ZS and HS have been analyzed to understand their oxidation mechanisms. The XRD patterns obtained from the oxide scales formed on both the composites during isothermal exposure at 1300 °C for 24 h are depicted in Fig. 6. The results in this figure indicate that the phases present in the oxide scale of ZS are tetragonal (t-) and monoclinic (m-) ZrO_2 as well as $ZrSiO_4$. Comparison of the peaks of t-ZrO_2 in the XRD patterns from oxide scales formed on ZS due to exposures for 24 and 100 h has shown that their intensities are higher for greater time of exposure. It may also be noted that

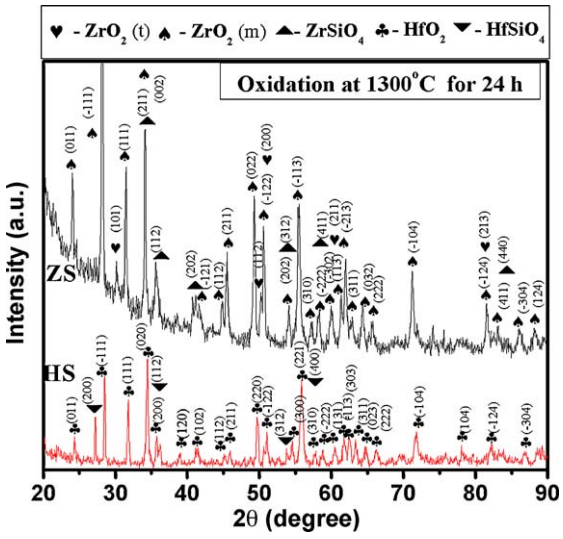

Fig. 6. XRD patterns obtained from the oxide scales formed on ZS and HS during isothermal oxidation tests in air at 1300 °C for 24 h.

the peaks of $ZrSiO_4$ could not be found in the XRD pattern from the oxide scale formed on ZS at 1200 °C. Similar to the results observed for the oxidized ZS, the XRD pattern (Fig. 6) obtained from the oxide scale of HS shows the peaks of HfO_2 (monoclinic) and $HfSiO_4$. Examination of oxide scales of both the composites by EDS and WDS microanalyses using SEM and EPMA, respectively have provided evidence for presence of a significant amount of SiO_2, in addition to the oxides detected by XRD studies. Hence, absence of the peaks of SiO_2 in the XRD pattern is attributed to its amorphous nature.

The SEM images depicting the top surfaces of the oxide scales formed on ZS subjected to exposure at 1200 and 1300 °C for 1 h are shown in Fig. 7(a) and (b), respectively. Magnified views of the selected locations in these images are shown as insets. Comparison of these images shows the oxide scale formed on ZS at 1200 °C to be rougher and more granular in comparison to that formed at 1300 °C. Both these oxide scales appear porous, with the average pore size being higher in case of the oxide scale formed at higher temperature. A typical EDS spectrum from bulk of the oxide scale formed on exposure at 1300 °C for 24 h shows the peaks of O, Zr, Si, C and B, which is suggestive of the presence of ZrO_2, SiO_2 and B_2O_3. Furthermore, the presence of the peak of C in the EDS spectrum is attributed to the presence of unoxidized SiC beneath the scale. The relatively smooth regions within the higher magnification insets in Fig. 7(a) and (b) have been found by EDS analysis to contain B_2O_3–SiO_2, which has a fine dispersion of ZrO_2 particles. Cracks and discontinuities are clearly visible in these locations of the oxide scale.

Typical SEM images depicting the top surfaces of oxide scales formed on ZS by exposure at 1200 and 1300 °C for 24 h are shown in Fig. 8(a) and (b), respectively. Examination of these images shows: (i) the presence of a smooth SiO_2-rich region with sub-micrometer size grains of ZrO_2 sticking to it, as confirmed by observations at higher magnification [inset in Fig. 8(a)] as well as EDS analysis; and (ii) flakes of SiO_2 with flower-type appearance scattered in the smooth matrix. Furthermore, comparison of Fig. 8(a) and (b) indicates that density of

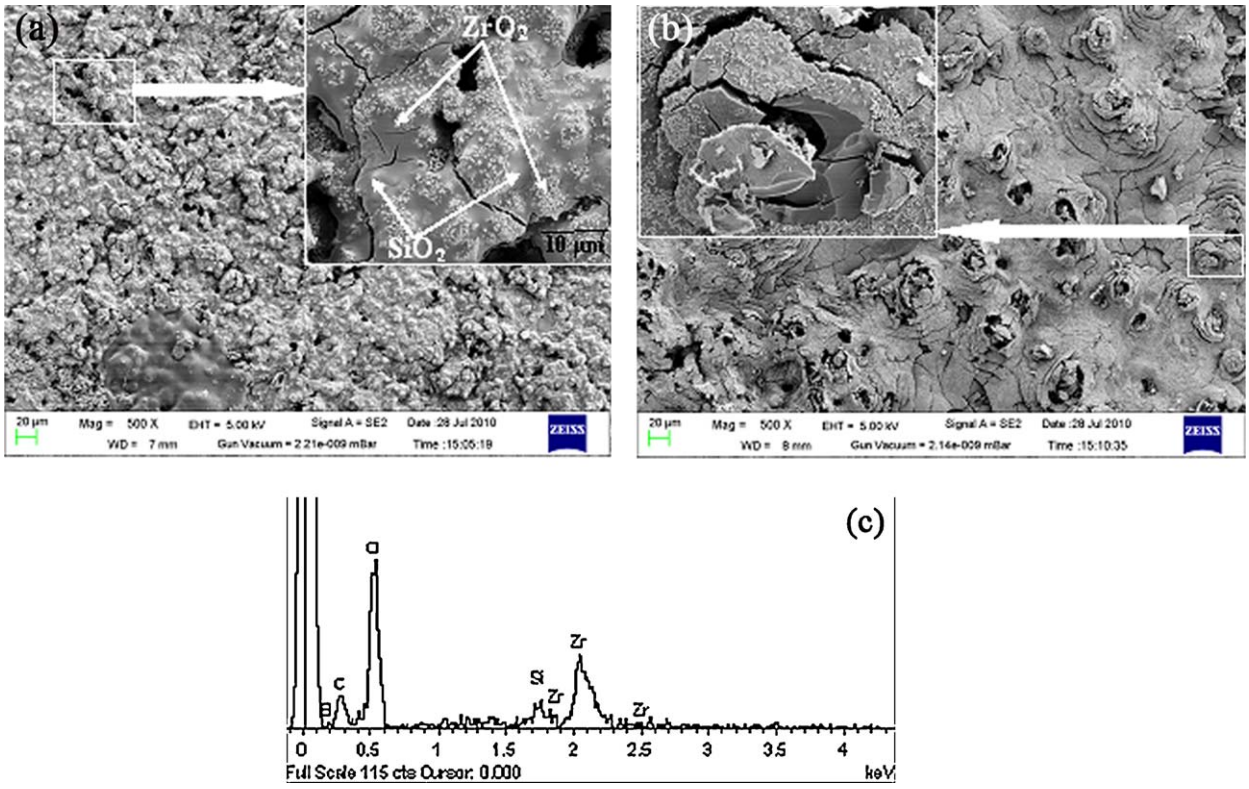

Fig. 7. SEM micrographs depicting the top surfaces of the oxide scales formed by isothermal oxidation of ZS for 1 h in air at: (a) 1200 °C, and (b) 1300 °C; as well as (c) EDS spectrum from bulk of the oxide scale showing peaks of O, Zr, Si, C and B. Insets in (a) and (b) show these locations at higher magnification.

these flower-type locations, average size of SiO_2-rich flakes, and number of flakes with cracks are much greater in the oxide scale formed at 1300 °C than that at 1200 °C. Observation of the surfaces of SiO_2-based flakes at higher magnification [inset in Fig. 8(b)] and EDS analysis has shown the presence of flat button-shaped ZrO_2 particles clustered at different locations of the smooth SiO_2-rich matrix. Comparison of the oxide scales formed after 1 h [Fig. 7(a)] and that after 24 h [Fig. 8(a)] of exposure at 1200 °C shows the latter scale's surface to be smoother and with much less porosity. However, the oxide scales formed at 1300 °C on exposure for both 1 and 24 h appear to have similar flower-like features, except for the fact that the scale formed on exposure for shorter period appears to have smaller flower-shaped features and much higher amount of porosity.

A typical SEM (SE) image depicting the cross-section of the oxide scale formed on ZS by exposure at 1200 °C for 24 h is shown in Fig. 9(a), and EDS X-ray maps of Zr, O and Si are shown in Fig. 9(b) through (d), respectively. Examination of this figure indicates that the oxide scale is made of a more or less continuous SiO_2-rich layer at the top, which is followed by a layer containing a mixture of ZrO_2 and SiC particles. An EPMA (BSE) image depicting the cross-section of the oxide scale formed on ZS by exposure at 1300 °C for 100 h is presented in Fig. 10(a). A network of cracks is visible in this image, depicting the oxide scale formed on ZS by exposure at 1300 °C for 100 h. Furthermore, the WDS X-ray maps of Zr, O, Si and B, as shown in Fig. 10(b) through (e), respectively indicate the presence of an outer layer of B_2O_3–SiO_2 and an inner layer comprising ZrO_2–SiC mixture.

Typical SEM images depicting the top surfaces of oxide scales formed on HS due to exposure for 1 h at 1200 and 1300 °C are shown in Fig. 11(a) and (b), respectively, with magnified views of selected locations as insets. Examination of these images shows much higher smoothness and lower area fraction of porosities in the oxide scale formed at the higher temperature. Examination of these insets shows presence of cracks around the pores. Furthermore, the top surfaces of the oxide scales formed on HS due to exposure at 1200 and 1300 °C for 24 h are depicted in the SEM (SE) images presented in Fig. 12(a) and (b), respectively. Careful examination of these images shows grains of HfO_2 sticking to relatively smooth matrix of SiO_2, with the area fraction of the former oxide being much greater in the oxide scale formed by exposure at the higher temperature. Further observations of these oxide scales at higher magnification have confirmed that the sizes of HfO_2 grains formed at 1300 °C are ~5–10 times greater than that formed on oxidation at 1200 °C. It should also be noted that the images of oxide scales formed on exposure at 1200 or 1300 °C for 24 h (Fig. 12) shows absence of porosities, unlike that observed on the surfaces of the sample exposed for 1 h (Fig. 11). Moreover, the volume fraction of HfO_2 is found to be much greater in the oxide scale of HS exposed at either 1200 or 1300 °C for 24 h than that after 1 h of exposure.

A typical SEM (SE) image depicting the cross-section of oxide scale formed on HS on exposure at 1200 °C for 24 h is shown in Fig. 13(a), and EDS X-ray maps of Hf, O and Si are shown in Fig. 13(b) through (d), respectively. Examination of this figure suggests that a more or less continuous SiO_2-rich

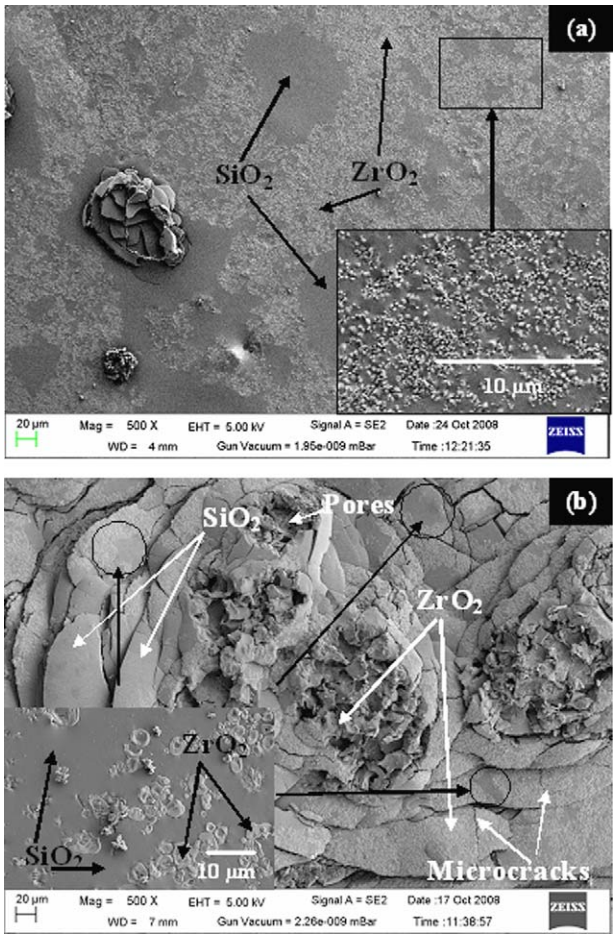

Fig. 8. SEM micrographs depicting the top surfaces of the oxide scales formed by isothermal oxidation of ZS for 24 h in air at: (a) 1200 °C, and (b) 1300 °C. Insets in (a) and (b) show these locations at higher magnification.

layer is developed on HS after 24 h of isothermal exposure at 1200 °C. Typical structure of the cross-section of the oxide scale formed on HS by exposure at 1300 °C for 100 h is shown in Fig. 14(a), while the WDS X-ray elemental maps of Hf, O, Si and B are shown in Fig. 14(b) through (e). The oxide scale of HS as shown in 14(a) appears to have crack density much less than that in oxide scale of ZS subjected to similar oxidation test. The elemental X-ray maps in these figures confirm the presence of an outer layer of B_2O_3–SiO_2, and an inner layer containing HfO_2–SiC phase mixture. These layers have been found in the oxide scales of HS formed at both 1200 and 1300 °C on either 24 or 100 h of exposure.

The thicknesses of individual layers of the oxide scales formed on ZS and HS by exposure at 1200 or 1300 °C for 24 or 100 h, as assessed by analyzing different SEM and EPMA images of cross-sections are shown in Table 1. Comparison of the results in this table pertaining to the oxide scales of ZS exposed for 24 or 100 h at 1200 and 1300 °C, indicates that the SiO_2-rich top layers have almost similar thicknesses for both the temperatures, while the layer containing mixture of ZrO_2 and SiC is ~2.5 times thicker at the higher temperature. However, both these layers in the oxide scale of ZS exposed at either of the investigated temperatures for 100 h show significantly higher thickness compared to that found after 24 h. Moreover, the thicknesses of unoxidized fractions are found to be reduced by 26.3% and 28.5% at 1200 and 1300 °C, respectively on increasing the time of exposure from 24 to 100 h. On the other hand, the changes in thickness of unoxidized portions of HS specimens are not very significant, although there is a modest change in thicknesses of the constituent layers in the oxide scales on increase in time of exposure from 24 to 100 h. Much smaller change in thickness of unoxidized part of HS than that of ZS with increase in the temperatures or time of exposure is consistent with the observed lower mass gain during isothermal exposure of the former composite (Figs. 4 and 5).

Studies of cross-sections of the oxide scales formed on subjecting to 24 1 h cycles of exposures at 1300 °C by SEM and EDS X-ray elemental mapping have shown the structure to be similar to that obtained by isothermal exposures. The SEM (SE) images depicting the morphologies of the top surfaces of oxide scales formed on ZS and HS by cyclic oxidation are shown in Fig. 15(a) and (b), respectively. The flower-like patterns observed in the oxide scale of ZS subjected to cyclic oxidation [Fig. 15(a)] appear similar, but much larger in size than that found in the scales formed by isothermal exposure at 1300 °C [Fig. 8(b)]. Further examination of this figure shows that the SiO_2-rich flakes in these flower-like patterns possess a random distribution of microcracks, and granular ZrO_2 is exposed to air by disintegration of these flakes. On the other hand, the SEM image [Fig. 15(b)] depicting the oxide scale formed by cyclic exposures of HS shows the presence of granular HfO_2-rich islands embedded in relatively smooth SiO_2-rich matrix with scattered porosities. A close comparison of Fig. 15(b) with Fig. 12(b) indicates that the area fraction of HfO_2 is much greater in the former scale. Examination of the selected areas with porosities at higher magnification [Fig. 15(c)] shows evidence for rupture and localized spallation of the scale, with HfO_2 grains (presence of Hf and O confirmed by EDS analysis) having much greater average size and wider size distribution (≤0.5–1.5 μm) present underneath, than that embedded on the top surface. Thus, it may be proposed that the HfO_2 grains grow in size with increasing time of exposure, while the oxide scale grows beyond these grains.

3.3.2.2. Residual stress. The stability of oxide scales formed during cyclic exposures depends on their resistance to damage due to internal stresses developed during exposure to thermal cycles. Table 2 shows the biaxial principal residual stresses, σ_1 and σ_3, as well as the maximum shear stress, τ_{max} [$=(\sigma_1-\sigma_3)/2$] generated within m-ZrO_2 and HfO_2 phases present in the oxide scales of ZS and HS, respectively. The residual strain caused by the CTE mismatch ($\Delta\alpha$) for a temperature drop of ΔT is given by the following expression:

$$\varepsilon = \Delta\alpha \cdot \Delta T \tag{1}$$

Hence, the biaxial residual stress, σ developed in a given phase at the end of a single thermal cycle is obtained from the following relationship:

$$\sigma = \left[\frac{E}{1-\nu}\right][\Delta\alpha \cdot \Delta T] \tag{2}$$

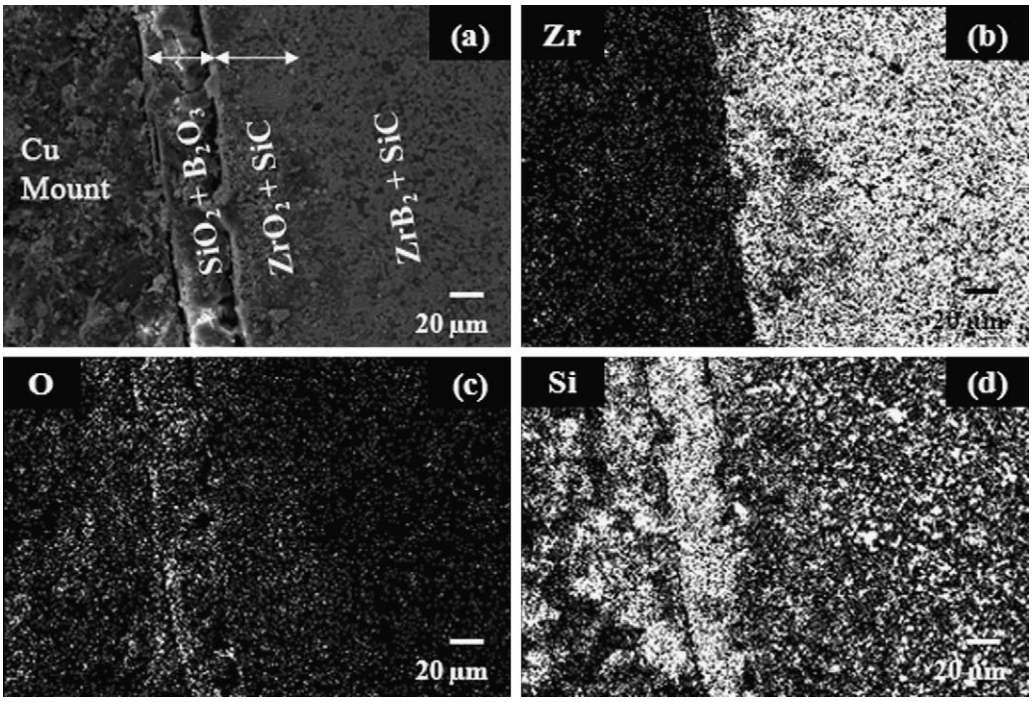

Fig. 9. Cross-section of the oxide scale formed on ZS by exposure for 24 h at 1200 °C: (a) SEM (BSE) image, as well as EDS X-ray maps of: (b) Zr, (c) O, and (d) Si. The boundaries between different layers are shown with arrows.

Table 1
Thicknesses of pre-oxidized specimens, unoxidized part of specimens, and the layers within the oxide scales formed on ZS and HS, subjected to exposure at 1200 or 1300 °C for 24 or 100 h.

Composite	Conditions of exposures: temperature–time	Thickness of:			
		Pre-oxidized sample (μm)	Unoxidized material (% of initial thickness)	$SiO_2 + B_2O_3$ layer (μm)	$HfO_2/ZrO_2 + SiC$ layer (μm)
ZS	1200 °C–24 h	4000	95.5	34 ± 4	56 ± 1
ZS	1200 °C–100 h	3200	69.25	233 ± 11	259 ± 9
ZS	1300 °C–24 h	4000	91.25	36 ± 2	139 ± 1
ZS	1300 °C–100 h	4100	62.73	375 ± 40	389 ± 30
HS	1200 °C–24 h	4000	97.95	15 ± 5	26 ± 1
HS	1200 °C–100 h	3940	96.93	26.9 ± 5	33.5 ± 7
HS	1300 °C–24 h	3900	96.97	25 ± 4	34 ± 1
HS	1300 °C–100 h	3800	96.63	29.4 ± 3	35 ± 1.5

where E is the Young's modulus and ν is the Poisson's ratio. The values of residual stress have been calculated by assuming that ZrO_2 and HfO_2 phases in the oxide scales of ZS and HS, respectively are surrounded by amorphous SiO_2 phase, which is also evident from the SEM images in Fig. 15(a) and (b). The results in Table 2 indicate the following facts: (i) the signs of one and both principal stresses measured experimentally for ZrO_2 and HfO_2, respectively as well as the calculated stress are positive, confirming that these stresses are tensile; and (ii) both the calculated and experimentally obtained values of residual stress for HfO_2 are higher than that for ZrO_2. A tensile residual stress in ZrO_2 or HfO_2 is suggestive of compressive stress in the surrounding SiO_2.

3.3.3. Microhardness

Plots depicting the variation of microhardness with distance from the oxide scale-composite interface, as fraction of specimen thickness, are shown in Fig. 16. These plots show the

Table 2
Biaxial principal residual stresses, σ_1 and σ_2, and maximum residual shear stress, τ_{max}, present in the selected phases of oxide scales of ZS and HS subjected to cyclic oxidation at 1300 °C. Values of stress calculated from Eq. (2) are also shown for comparison.

Composites	Phase and plane ($h\,k\,l$)	σ_1 (MPa)	σ_2 (MPa)	τ_{max} (MPa)	Calculated stress (MPa)
ZS	ZrO_2 ($\bar{1}\,1\,1$)	459.2	−5.8	232.5	1700
HS	HfO_2 ($\bar{1}\,1\,1$)	573.5	247.0	410.25	1775.89

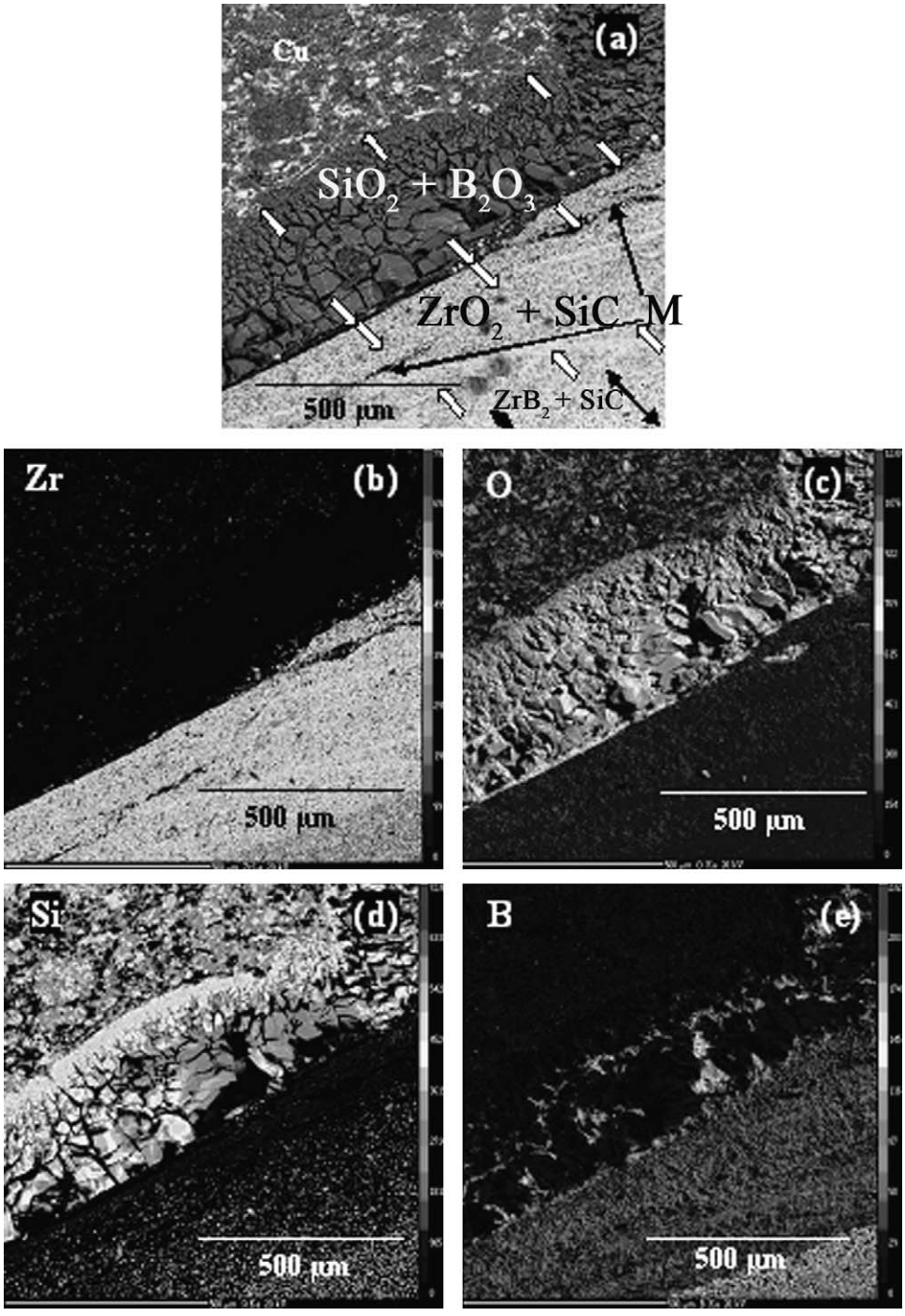

Fig. 10. Cross-section of the oxide scale formed on ZS by exposure for 100 h at 1300 °C: (a) EPMA (BSE) image, as well as WDS X-ray maps of: (b) Zr, (c) O, (d) Si and (e) B. Interlayer boundaries within the oxide scale are shown with arrows. A microcrack beneath the outer layer of the oxide scale is shown with an arrow, and is labelled as “M”.

following results: (i) the microhardness decreases, as one proceeds from the centre to composite-oxide scale interface; (ii) at a given position, lower microhardness is observed for the sample subjected to cyclic oxidation than that tested isothermally; (iii) the drop in microhardness of ZS or HS near the oxide scale is much higher on isothermal exposure for 100 h than that for 24 h; and (iv) the span of low microhardness for ZS is significantly greater than that for HS on subjecting to isothermal exposure at 24 or 100 h, while the trend is reversed for cyclic exposures.

4. Discussion

4.1. Oxidation reactions

Examination of the products of oxidation indicates that the reactions involved in oxidation of ZS and HS are as follows:

$$(2/5)ZrB_2\,(s) + O_2\,(g) \rightarrow (2/5)ZrO_2\,(s) + (2/5)B_2O_3\,(l) \quad (3)$$

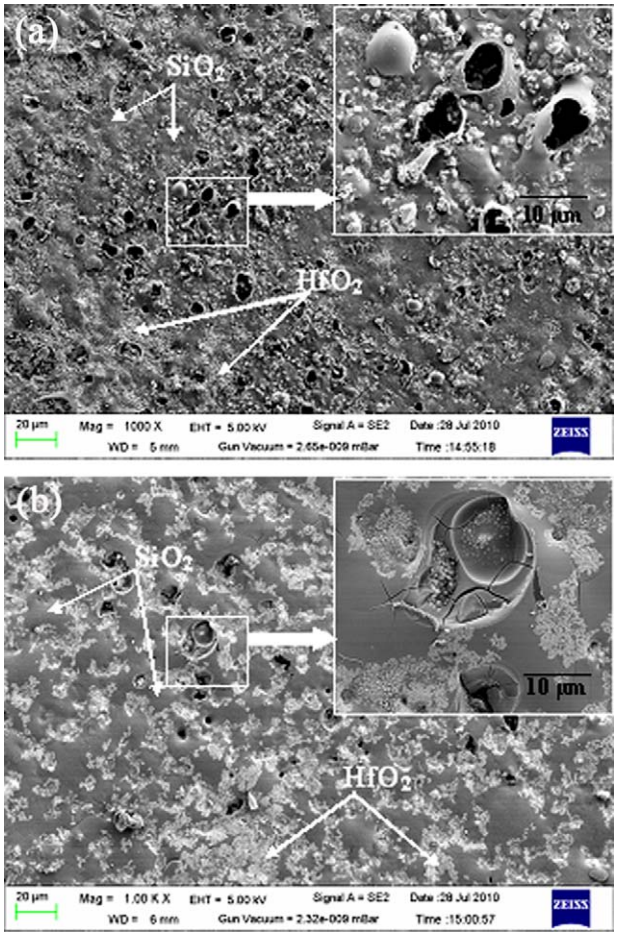

Fig. 11. SEM micrographs depicting the top surfaces of the oxide scales formed by isothermal oxidation of HS for 1 h in air at: (a) 1200 °C, and (b) 1300 °C. Insets in (a) and (b) show these locations at higher magnification.

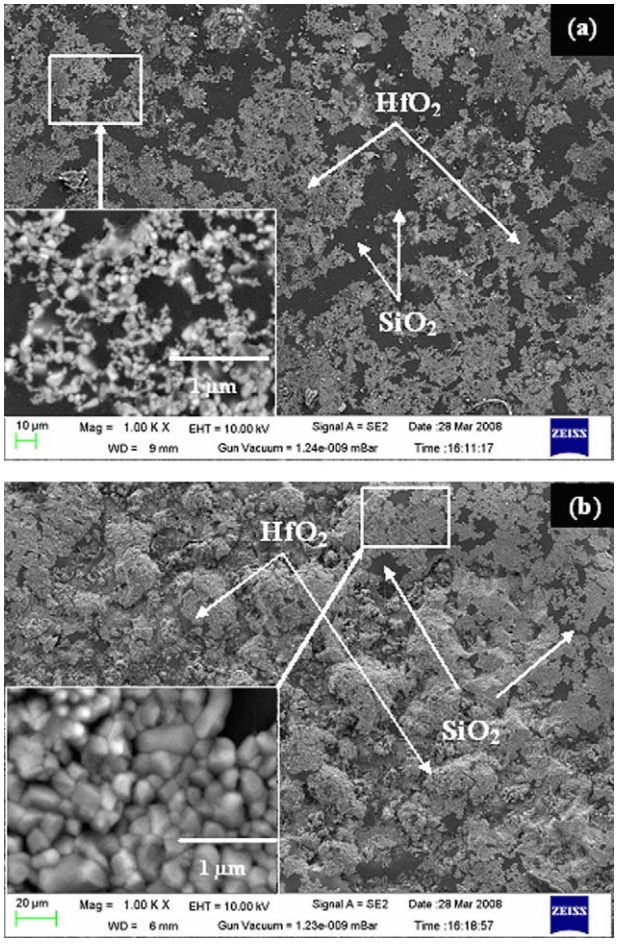

Fig. 12. SEM micrographs depicting the top surfaces of oxide scales formed by isothermal oxidation of HS for 24 h in air at: (a) 1200 °C, and (b) 1300 °C. Insets in (a) and (b) show HfO_2 grains at higher magnification.

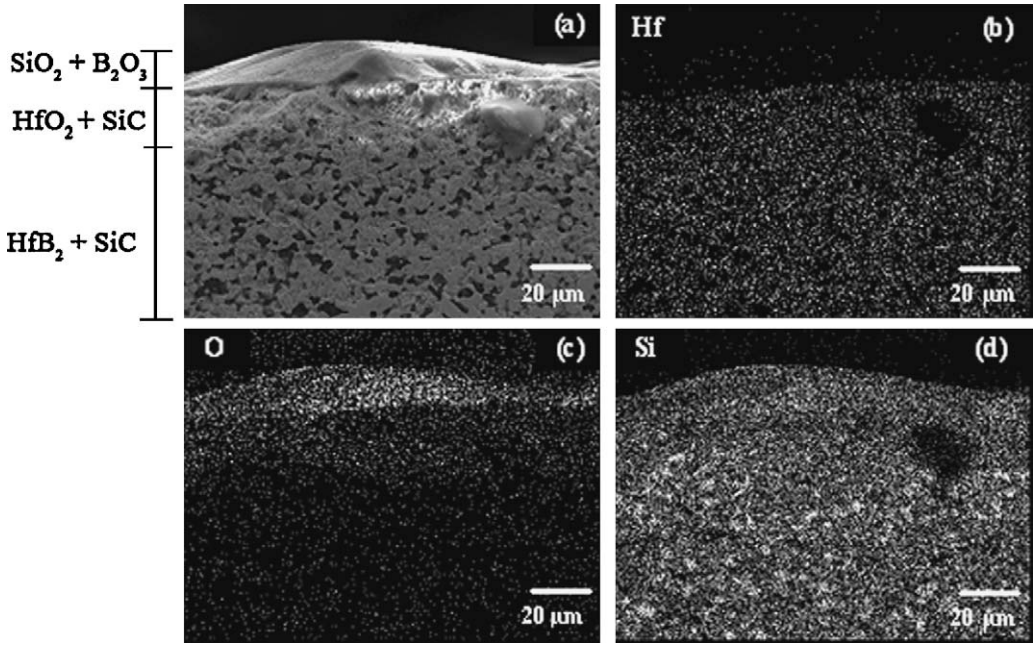

Fig. 13. Cross-section of the oxide scale formed on HS by exposure for 24 h at 1200 °C: (a) SEM (BSE) image, as well as EDS X-ray maps of: (b) Hf, (c) O, and (d) Si. Limits of the oxide scale are shown with arrows.

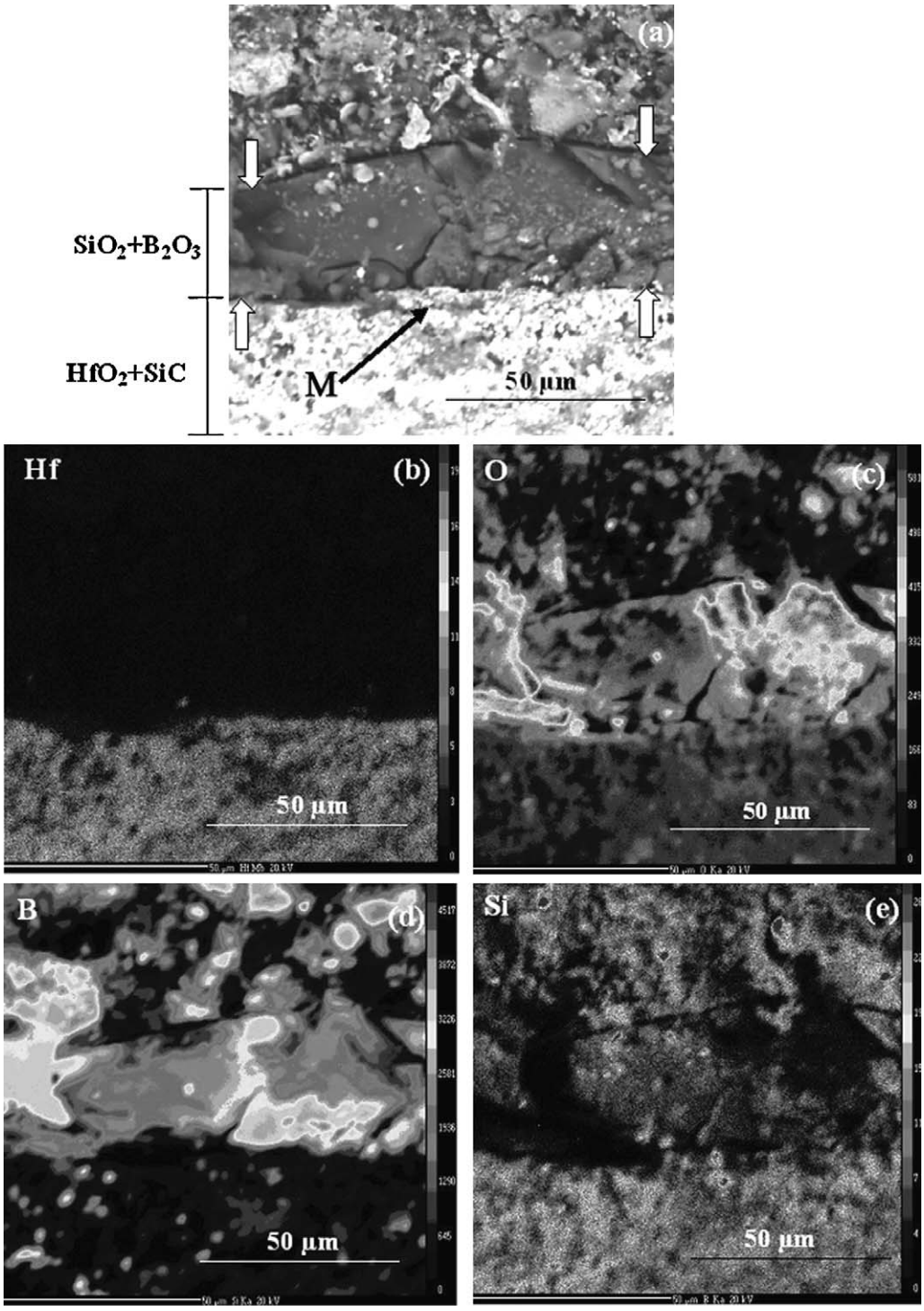

Fig. 14. Cross-section of the oxide scale formed on HS by exposure for 100 h at 1300 °C: (a) EPMA (BSE) image, as well as WDS X-ray maps of: (b) Hf, (c) O, (d) Si and (e) B. A microcrack beneath the outer layer of the oxide scale is marked as “M”.

$$ZrO_2\,(s) + SiO_2\,(s) \rightarrow ZrSiO_4\,(s) \quad (4)$$

$$(2/5)HfB_2\,(s) + O_2\,(g) \rightarrow (2/5)HfO_2\,(s) + (2/5)B_2O_3\,(l) \quad (5)$$

$$HfO_2\,(s) + SiO_2\,(s) \rightarrow HfSiO_4\,(s) \quad (6)$$

$$(2/3)SiC\,(s) + O_2\,(g) \rightarrow (2/3)SiO_2\,(l) + (2/3)CO\,(g) \quad (7)$$

$$SiC\,(s) + O_2\,(g) \rightarrow SiO\,(g) + CO\,(g) \quad (8)$$

$$B_2O_3\,(l) \rightarrow B_2O_3\,(g) \quad (9)$$

The Reactions (3)–(8) have been found to be feasible on the basis of calculations of free energy change per mole of oxygen (ΔG).[32]

The equilibrium constants (K_{eq}) for the Reactions (3), (5) and (7) have been calculated from the values of ΔG using the

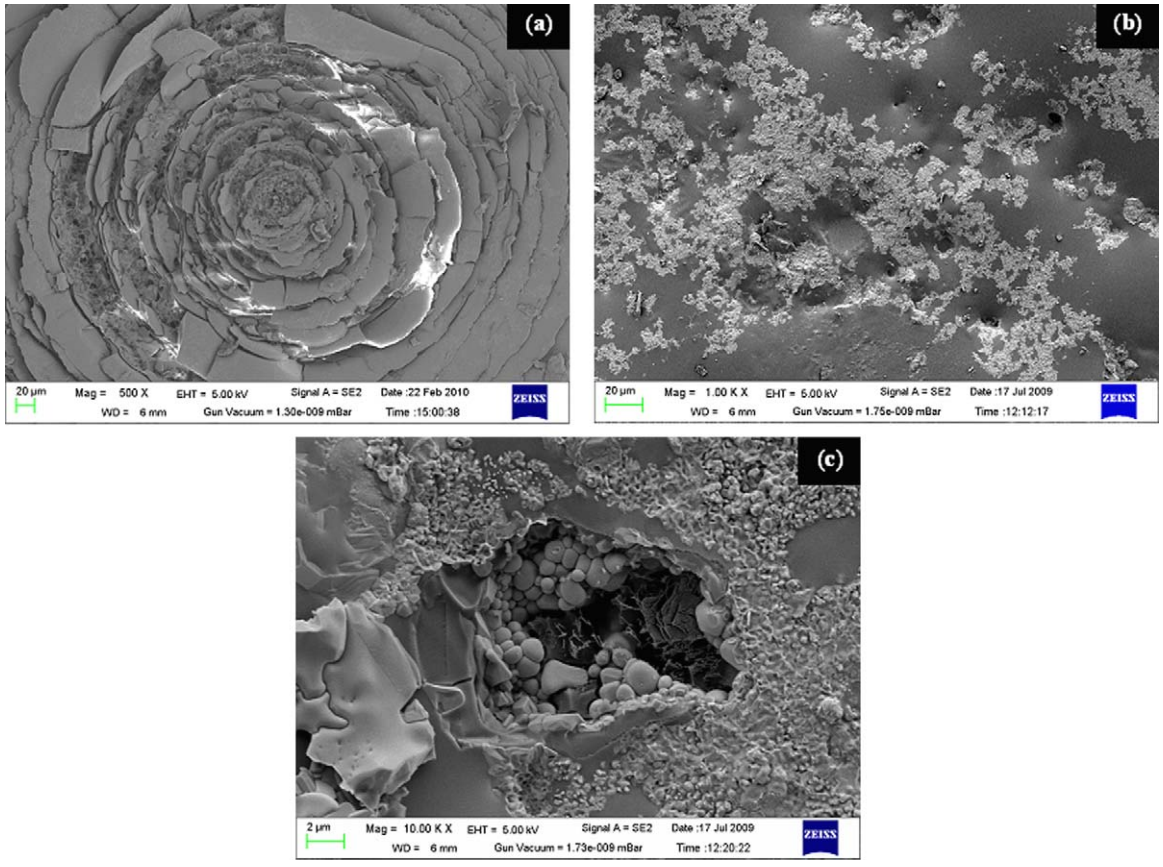

Fig. 15. SEM micrographs depicting the top surface of oxide scale formed by cyclic oxidation for 24 h in air at 1300 °C on: (a) ZS, (b) HS at low magnification, and (c) HS at high magnification. Porosities can be observed in the granular ZrO_2-rich region in (a), while evidence for spallation of HfO_2 is visible in (c).

following relationship:

$$\Delta G = -RT \ln K_{eq} \tag{10}$$

where R is the ideal gas constant and T is the absolute temperature. The values of K_{eq} (with reaction numbers as subscripts) are expressed as:

$$K_{3eq} = \frac{[(a_{ZrO_2})^{2/5} \times (a_{B_2O_3})^{2/5}]}{[(a_{ZrB_2})^{2/5} \times (p_{O_2})]} \tag{11}$$

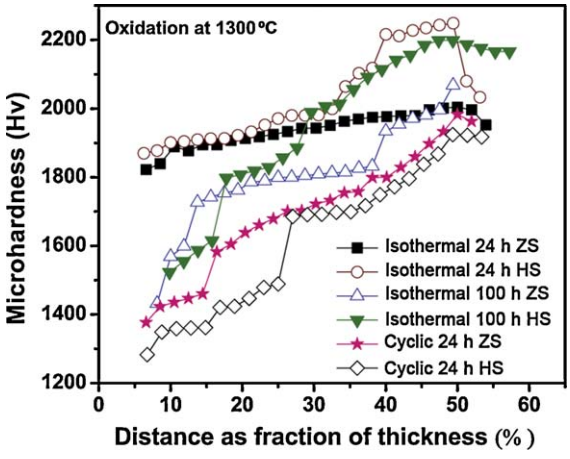

Fig. 16. Plots showing variation of microhardness with distance from interface of oxide and composite as fraction of thickness of the sample.

$$K_{5eq} = \frac{[(a_{HfO_2})^{2/5} \times (a_{B_2O_3})^{2/5}]}{[(a_{HfB_2})^{2/5} \times (p_{O_2})]} \tag{12}$$

$$K_{7eq} = \frac{[(a_{SiO_2})^{2/3} \times (p_{CO})^{2/3}]}{[(a_{SiC})^{2/3} \times (p_{O_2})]} \tag{13}$$

where a is the activity of the species involved in the reactions and (p_{O_2}) is the equilibrium partial pressure. The values of ΔG and K_{eq} for 1227 °C (1500) calculated using Eq. (10), as well as p_{O_2} calculated by considering the activities of pure substances as unity from Eqs. (11) to (13) are compiled in Table 3. The calculation for Reaction (7) has been carried out by ignoring the presence of CO, as has been done earlier for oxygen partial pressures greater than that for the SiC–SiO_2 equilibrium.[33] The results in this table indicate that (i) $\Delta G_5 < \Delta G_3 < \Delta G_7$ at 1227 °C, and (ii) the value of p_{O_2} required for oxidation of HfB_2 is an order of magnitude less than that for ZrB_2. The thermodynamic data in Table 3 clearly indicates that the driving force for oxidation at 1227 °C increases in the following order:

Table 3
Thermodynamic data for Reactions (3), (5) and (7) at 1227 °C (1500 K).

Reactions	ΔG (kJ/mol)	K_{eq}	p_{O_2} (atm)
3	−587.6	8.94×10^{19}	1.12×10^{-20}
5	−602.0	2.82×10^{20}	3.55×10^{-21}
7	−557.1	1.58×10^{19}	6.3×10^{-20}

$SiC < ZrB_2 < HfB_2$. However, the observation of greater mass gain and higher SiO_2-rich layer thickness in the oxide scale for the ZS than that for the HS contradicts the expectations from the above-mentioned thermodynamic data. Such deviation under isothermal conditions of exposure may be attributed to higher rate of diffusion through the oxide scale of ZS than through that of HS.[20]

Through calculations using atomic mass, it is obvious that the Reactions (3), (5) and (7) are responsible for net mass gain, while the Reactions (8) and (9) contribute to mass loss. The mass gain (considering B_2O_3 in liquid form) through Reactions (3), (5) and (7) are +32, +32 and +13.33 a.m.u., respectively, while the loss due to volatilization of B_2O_3 is calculated as −27.84 a.m.u. Thus, it may be inferred that there is net mass gain even after volatilization of the entire amount of B_2O_3 produced through the Reactions (3) and (5). It should be noted that the Reaction (8) provides the mechanism for active oxidation of SiC, as has been discussed in the literature.[3,35] Although this reaction is thermodynamically feasible, the accompanying decrease in free energy ($\Delta G = -411.68$ kJ/mol) is less than that for the Reaction (7) (Table 3), indicating that the latter reaction is more preferable under the present experimental conditions. Moreover, it has been shown through experiments and theoretical calculations that the active oxidation of SiC is marginal at 1200 °C in dry air,[34] and is promoted in reducing atmospheres containing CO–CO_2 or H_2–H_2O gas mixtures along with low oxygen partial pressures.[35]

4.2. Early stages of oxidation

The results of thermogravimetric analysis indicate that the process of oxidation begins for both ZS and HS at specific temperatures in course of heating. The mass gain observed for ZS between 740 and 1200 °C is attributed to oxidation of ZrB_2, leading to the formation of ZrO_2 and B_2O_3 (Reaction (3)), as suggested by Rezaie et al.[16] The oxidation of the ZrB_2 matrix is preferred to that of SiC, as predicted by the results of thermodynamic calculations shown in Table 3. Abrupt increase in mass gain observed for ZS above 1200 °C (Fig. 2) suggests that there is a significant increase in the oxidation rate of the ZrB_2 matrix along with initiation of oxidation of SiC particles, in agreement with the results of earlier studies.[15,36] As the B_2O_3 (l) begins to evaporate, the oxide scale becomes unprotective, which is obvious from its surface morphology showing bubbles and pores after exposure for 1 h at 1200 or 1300 °C (Fig. 7). As unrestricted ingress of oxygen from the atmosphere is permitted through the porous oxide scale, the Reactions (3) and (7) are able to progress in an unabated manner. In an earlier study,[36] the oxidation of micrometer-size SiC particles has been reported to begin at 843 °C in course of heating in the TGA at the rate of 10 °C/min. However, the oxidation of SiC in the ZrB_2–SiC composite has been reported to occur at temperatures >1100 °C,[2] although its rate is known to be less than that of ZrB_2 till about 1200 °C.[36] The slower rate of oxidation of SiC in ZS or HS than that in its powder form is partly attributed to greater surface area of the latter type of material.

Vaporization of B_2O_3 at temperatures ≥1100 °C,[6,15] and its escape along with that of CO (g) (formed by oxidation of SiC) appears to have the most significant contribution to the formation of porosities. Furthermore, based on a model proposed by Parthasarathy et al.,[22] it may also be suggested that monoclinic to tetragonal transformation of ZrO_2 above 1170 °C involving volume shrinkage of ∼3–6%, leads to the creation of porosities. Creation of porosities makes it easier for the atmospheric oxygen to reach the oxide–material interface, and further oxidation of both SiC and ZrB_2 is promoted, until a protective SiO_2-rich scale (Fig. 9) is formed after exposure for a period of ∼24 h.

The initiation of mass gain in HS at 500 °C is attributed to the start of oxidation of HfB_2 (Reaction (5)), and increase in its rate beyond 700 °C is consistent with the expected trend. The mass loss observed for the HS at temperatures >1100 °C is similar to that reported for the hot pressed HfB_2–SiC composite by Moteverde and Bellosi,[8] who have attributed it loss of volatile oxidation products. This mass loss is less than the total mass gain, such that the net mass change is not negative. If escape of B_2O_3 (g) is considered as the reason for mass loss, a net mass gain is expected from the calculations of mass change from Reactions (5) and (7), as discussed in Section 4.1, which is in agreement with the results shown in Fig. 2. It has been reported by Lespade et al.[38] that most of the B_2O_3 (l) in the oxide scale is vaporized beyond 1100 °C, and significant mass gain by oxidation of SiC is expected at ∼1200 °C or above. In fact, mass gain has been reported by Moteverde and Bellosi[8] at temperatures exceeding 1250 °C, indicating the regime of mass loss as transient and related to sudden excessive vaporization of B_2O_3 (g). Probably, no mass gain has been found in the present study carried out till 1300 °C, as the heating rate was 10 times more than that used by Moteverde and Bellosi.

The results related to the early stages (<30 min) of isothermal exposure of HS at 1200 or 1300 °C have been found to differ from that of ZS in two ways. First, mass loss has been observed for HS (Fig. 3), while only mass gain has been recorded for ZS. Second, the oxide scale formed on ZS [Fig. 7(a) and (b)] appears rougher and more granular than that on HS [Fig. 11(a) and (b)] at the same temperature, indicating that the rate of formation of HfO_2 is substantially less that of ZrO_2. The negative mass change observed for HS during its initial stage of exposure at 1200 °C is partly in tune with mass loss observed during non-isothermal tests (Fig. 2).

The first observation mentioned above suggests that the Reaction (5) leading to mass gain in HS is retarded during heating or during the initial stages of isothermal oxidation at 1200 or 1300 °C, which can only be possible due to temporary protection by B_2O_3–SiO_2 scale together with lower diffusivity of oxygen anions through HfO_2.[22] Larger area fraction of SiO_2 in oxide scale of HS than that in ZS, as is evident by comparison of the oxide scale surfaces (Figs. 7, 8, 11 and 12), can be considered as evidence for slower growth of HfO_2 than ZrO_2.

The presence of several micrometer-size pores on the surfaces of oxide scales formed on HS exposed for 1 h at 1200 °C as shown in Fig. 11(a), can be considered as evidence for the escape of volatile gaseous products. Formation of SiO and CO by active oxidation of SiC through Reaction (8) is a possibility, which is

ruled out under the prevailing conditions of oxidation, based on information from literature.[3,34,36,37] It is intuitive that vaporization of B_2O_3 (l) already present in the oxide scale through Reaction (9) is independent of the instantaneous rate of the Reaction (5), and therefore it can have significant effect on reduction in net mass gain, as has been observed during non-isothermal oxidation. However, loss of B_2O_3 (g) and CO (g) cannot be used to account for the negative mass changes during the initial period of isothermal oxidation of HS, because of the net mass gain through Reactions (5) and (7) as expected from the results of calculations mentioned in Section 4.1. Hence, localized spallation during the rupture of bubbles on the viscous B_2O_3–SiO_2 scale along with loss of gaseous products is considered as the reason contributing to mass loss in HS during the initial stages of isothermal exposure at 1200 or 1300 °C. The effect of rupture and spallation are not observed to such an extent during isothermal oxidation of ZS, because the escape of gaseous products is made easy by typically porous ZrO_2, which has higher growth rate than SiO_2. It should be noted that the effect of spallation on mass changes could not be noticed during non-isothermal oxidation tests, as the samples were kept inside alumina crucible.

4.3. Oxide scale morphology and internal stresses

The scale of amorphous B_2O_3–SiO_2 on ZS or HS is known to be protective, as its fluidity (greater than that of SiO_2) and visco-plastic flow aids in sintering of the oxide scale with closure of pores, which is evident on examination of a nearly continuous top layer of B_2O_3–SiO_2 (Figs. 9 and 13), which appears as smooth locations on the corresponding top surfaces [Figs. 8(a) and 12(a)]. During the initial stages of exposure at 1200 and 1300 °C, the amounts of mass gain or loss have been found to fluctuate sharply as shown in Fig. 3, because competitive formation and growth of ZrO_2 or HfO_2 with that of SiO_2–B_2O_3 tends to prevent the latter from becoming continuous and stable. The above argument can be defended logically by comparing the surfaces of oxide scales formed on either ZS or HS after 1 and 24 h of exposure at 1200 or 1300 °C. In both ZS and HS, the oxide scales formed by exposure at 1200 or 1300 °C for 24 h contain less porosity, and appear relatively smoother compared to that formed after 1 h period. Furthermore, smaller pore density in the oxide scale of HS exposed to 1300 °C for 1 h [Fig. 11(b)] than that in the scale formed at 1200 °C [Fig. 11(a)], and the larger fraction of SiO_2-rich smooth areas indicates that the kinetics of protective scale formation is enhanced at the higher temperature in this material.

The results of studies on oxidation kinetics indicate that it takes approximately 24 h for both ZS and HS to reach a stable regime, which is characterized by no apparent mass change being detected. This stable regime observed on exposure of HS for 24 h suggests the presence of an equilibrium between mass loss due to escape of B_2O_3 (g) + CO (g) and mass gain by formation of HfO_2 + SiO_2. As the differences between the thicknesses of unoxidized portions of oxide scales formed by 24 and 100 h of exposures (Table 1) have been found to be insignificant, it is appropriate to suggest that the a protective oxide scale is developed on HS after isothermal exposure of 24 h at 1200 or 1300 °C. Similar stable regimes in the kinetic plots of Mo–Si–B alloys showing zero mass change after an initial period of mass loss along with images of oxide cross-sections showing continuous layer of B_2O_3–SiO_2 at the top, has been considered as evidence for formation of scale with protective nature in some of the previous reports.[39,40]

It should be noted that the oxide scale is not completely stable in case of the ZS, as an increase in mass is observed after 43 and 66 h of exposure at 1200 [Fig. 5(a)] and 1300 °C [Fig. 5(b)], respectively. Such abrupt changes in mass are attributed to accelerated oxidation being facilitated probably by rupture of the protective scale at random locations and penetration of gaseous oxygen or surface diffusion of oxygen anions through cracks or pores formed in the oxide scale. Rupture of the oxide scale on the surface of ZS is believed to be promoted by nucleation of the gas bubbles of B_2O_3 (g) followed by build up of its vapor pressure with increase in time of exposure. Examination of the results in Fig. 10(e) provides evidence for enrichment of B inside the cracks or discontinuities within the oxide scale of ZS. Such a distribution of B suggests that these cracks provide short circuit paths for outward movement of B_2O_3 (l), which is followed by its vaporization at the surface. The movement of B_2O_3 (l) is most likely promoted by capillary action of the narrow channel-type network of cracks within the oxide scale, similar to that expected from the "solid pillars, liquid roof" type model proposed by Li et al.[21] and Parthasarathy et al.[22]

It is interesting to note that the oxide scale formed on ZS during isothermal exposure at 1300 °C has well-developed flower-type morphology, which is in agreement with the observations reported by Talmy et al.[41] However, it should also be noted that this feature is found to a much smaller extent in the scale developed at 1200 °C. Development of this morphology can be traced to the mechanisms of early stages of oxidation of this composite. In spite of the fact that the growth rate of SiO_2 is greater at 1300 °C than that at 1200 °C, the susceptibility of ZrB_2 to oxidation as well as the rates of formation and escape of B_2O_3 (g) + CO (g) are increased. Thus, bubbles are formed in the viscous B_2O_3–SiO_2 scale and then ruptured with escape of volatile products, which is followed by healing either by formation of fresh SiO_2 or by visco-plastic flow of the scale. The process of repeated rupturing and healing by formation of SiO_2 is expected to give rise to the flower-type (or cabbage-type[41]) appearance of the oxide scale surface on ZS [Figs. 8(b) and 15(a)]. It is intuitive that the amount of volatilization of B_2O_3 (l) followed by its escape in gaseous form is more at 1300 °C than that at 1200 °C, which can be considered as the reason for the concentration of pores being more on the surface of the oxide scale formed at the higher temperature, as is obvious by comparison of Fig. 8(a) and (b).

The cracks present in the SiO_2-rich smooth locations of oxide scales of ZS or HS [Figs. 7(a) and (b), 8(b), 10, 11(a) and (b), 14 and 15(a) and (c)] are believed to be generated by stresses associated with ionic diffusion,[42] growth of ZrO_2 or HfO_2, pressure exerted by CO (g) and volatile B_2O_3 (g) formed in subsurface locations, as well as volume changes associated with the formation of oxidation products.[43] The volume changes due to Reactions (3)–(7) have been calculated as 271.5%, −17.5%,

274.7%, −14.2% and 97.2%, respectively by considering the molar volume of reactants and products. However, it should be noted that the stresses generated isothermally at high temperature by the above-mentioned mechanisms are expected to be at least partially neutralized by visco-plastic flow of B_2O_3–SiO_2 scale.

Greater degradation of both the investigated composites has been observed on being subjected to 24 cycles of 1 h exposure at 1300 °C than by isothermal exposure for 24 h at the same temperature, as is evident from Figs. 5(b) and 16. This observation is attributed to generation of larger flaws in the oxide scales (Fig. 15) in course of cyclic oxidation. Generation of these flaws during thermal cycles may be attributed to either volume change during phase transformation of ZrO_2 or strains due to CTE mismatch between oxide scale constituents and substrate. It is well-known[44,45] that heating of ZS beyond 1170 °C involves monoclinic (m)-to-tetragonal (t) transformation of ZrO_2, which is accompanied by its volume contraction of 3–6% and generation of tensile residual stress in the surrounding SiO_2-rich matrix within the oxide scale. In contrast, cooling involves t → m transformations accompanied by volume expansion by the same amount with generation of compressive residual stress. Thus, it is inferred that the sign of dimensional change in ZrO_2 due to phase transformation during either heating or cooling is opposite to that of its thermal expansion or contraction, respectively. In other words, the residual stress components in the SiO_2 matrix due to phase transformation of ZrO_2 are partially neutralized by that caused by the CTE mismatch between these phases.

As plasticity of B_2O_3–SiO_2 is reduced on cooling from high temperature, stresses due to thermal shock during the cooling cycles are expected to have a strong contribution to generation of flaws in the oxide scale. Hence, the cracks found in the oxide scales of both ZS and HS subjected to thermal cycles involving air cooling are more likely to originate from stresses arising out of thermal mismatch between constituent phases than due to any other mechanism operative for isothermal exposure, as discussed above. The CTE of amorphous SiO_2 ($\alpha = 0.5 \times 10^{-6}/°C$) is less than that of m-ZrO_2 ($\alpha = 7 \times 10^{-6}/°C$) and HfO_2 ($\alpha = 4.4 \times 10^{-6}/°C$). As a result, the SiO_2 is expected to contract much less than either m-ZrO_2 or HfO_2 in the oxide scale of ZS or HS, respectively on air cooling from 1300 °C. Due to interfacial bonding, the particles of ZrO_2 or HfO_2 are restrained from contracting by the surrounding SiO_2 matrix. Hence, radial tensile residual stresses are introduced inside the particles of ZrO_2 or HfO_2, which is consistent with the results shown in Table 2.

Based on information from an earlier report,[46] it is noted that the substrates with ZrB_2 ($\alpha = 5.9 \times 10^{-6}/°C$) or HfB_2 ($\alpha = 7.6 \times 10^{-6}/°C$) as matrices have values of CTE much greater than that of amorphous SiO_2. Hence, it is inferred that these substrates undergo larger thermal expansion and contraction during heating and cooling, respectively than the amorphous SiO_2-rich top layer of the oxide scale. The above argument suggests that the amorphous SiO_2 scale is subjected to tensile residual stress during heating and compressive residual stress in course of the cooling cycle. Higher CTE mismatch of SiO_2 with HfB_2 than that with ZrB_2 can be used as a suitable explanation for higher residual stress in the oxide scale of HS than in ZS (Table 2). Thus, it is possible to explain the occurrence of greater spallation of oxide scale with loss of B_2O_3 (g) in case of HS than for ZS on subjecting to multiple thermal cycles between 1300 °C and room temperature.

Examination of the data in Table 2 indicates that the calculated values of residual stress for a single cycle are much higher than those obtained experimentally after multiple cycles. It is well-accepted that residual stresses are partially relieved by generation of cracks in the oxide scale. The stress relief caused by cracking during exposure to multiple thermal cycles appears to be the most acceptable explanation for the differences between calculated (for single cycle) and experimental (multiple cycles) values, as shown in Table 2.

4.4. Internal damage

The internal damage in the composites subjected to either isothermal or cyclic oxidation tests has been evaluated by recording the fall in microhardness on approaching the oxide scale-composite interface, as shown in Fig. 16. Decrease in microhardness of the composites close to their interfaces with oxide scales, with respect to that in the center of a given sample is suggestive of damage by formation of microcracks, as is evident from Fig. 10(a). The following inferences may be drawn form the results of microhardness measurements: (i) the amount of damage near the oxide scale is increased with time of isothermal exposure; (ii) the damaged region is much wider than oxide scale thickness for both isothermal and cyclic oxidation; (iii) internal damage on cyclic oxidation is more severe than that observed during isothermal exposure for either of the investigated composites; and (iv) HS is more resistant than ZS to bulk damage during isothermal oxidation, while this trend is reversed on subjecting to 8 or more 1 h cyclic exposures at 1300 °C followed by air cooling. The lower microhardness observed in bulk of the investigated composites subjected to cyclic oxidation than that in their isothermally oxidized samples is attributed to more severe thermal shock induced damage in case of the former type of test. Furthermore, the internal damage caused during isothermal exposure for 24 h or more is suggestive of penetration of oxygen through the outer oxide scale, and internal oxidation with formation of porosities and microcracks in the bulk of the oxidized samples.

5. Conclusions

A comparative study of non-isothermal, isothermal and cyclic oxidation behavior has been carried out on ZrB_2–20 vol.% of SiC and HfB_2–20 vol.% of SiC composites prepared by hot pressing. The investigations carried out on these composites include non-isothermal studies involving heating inside TGA up to 1300 °C, isothermal exposures at 1200 and 1300 °C for 1, 24 or 100 h, and cyclic oxidation involving 24 cycles of 1 h exposure at 1300 °C followed by air cooling. The following conclusions may be drawn from this study:

The results of non-isothermal oxidation studies have indicated that mass changes are initiated in ZS and HS at 740 and 500 °C, respectively. Accelerated mass gain has been found in ZS at temperatures >1200 °C due to higher rate of formation of ZrO_2 and SiO_2 than that of escape of B_2O_3 and CO. On the other hand, mass loss has been observed for HS on heating beyond 1100 °C due to reduced rate of formation of HfO_2, compared to loss of B_2O_3 and CO.

The results of isothermal oxidation studies have revealed that HS is more resistant to oxidation than ZS at both 1200 and 1300 °C. The main oxidation products of ZS and HS are ZrO_2 and HfO_2, respectively along with B_2O_3–SiO_2 glass. The oxide scale formed during isothermal exposure of HS has been found to be stable and protective after about 24 h of exposure, while that of ZS has been found to undergo cracking followed by healing, leading to further mass gain. The oxide scale of ZS is more susceptible to damage than that of HS because of partial tetragonal to monoclinic phase transformation in ZrO_2 during cooling.

The cyclic oxidation resistance for HS has been found to be worse than that of ZS owing to greater thermal residual stresses in the oxide scales of the former material, causing more cracking and spallation. The residual stress in ZrO_2 or HfO_2 has been found to be tensile in nature, while that in amorphous SiO_2 is compressive. The extent of damage from oxide scale to center of HS samples, as estimated by microhardness measurements along the cross-section, has been found to be more than ZS for cyclic oxidation (for 24 1 h cycles at 1300 °C), and vice-versa for isothermal oxidation tests (24 h at 1300 °C). The widths of degraded regions in samples subjected to either isothermal or cyclic oxidation have been found to exceed the thickness of their oxide scales.

Acknowledgements

The financial supports from Defence Research and Development Organization and Central Scientific and Industrial Research, New Delhi are gratefully acknowledged. The authors also express their sincere gratitude to technical personnel at the Central Research Facility and Electron Probe Microanalysis National Facility, Department of Geology and Geophysics at IIT Kharagpur.

References

1. Kuriakose AK, Margrave JL. The oxidation kinetics of zirconium diboride and zirconium carbide at high temperatures. *J Electrochem Soc* 1964;**111**:827–31.
2. Tripp WC, Graham HC. Thermogravimetric study of the oxidation of ZrB_2 in the temperature range of 800–1500 °C. *J Electrochem Soc* 1968;**118**:1195–9.
3. Fahrenholtz WG. The ZrB_2 volatility diagram. *J Am Ceram Soc* 2005;**88**(12):3509–12.
4. Opeka MM, Talmy IG, Wuchina EJ, Zaykoski JA, Causey SJ. Mechanical, thermal, and oxidation properties of refractory hafnium and zirconium compounds. *J Eur Ceram Soc* 1999;**19**:2405–14.
5. Levine SR, Opila EJ, Halbig MC, Kiser JD, Singh M, Salem JA. Evaluation of ultra high temperature ceramics for aeropropulsion use. *J Eur Ceram Soc* 2002;**22**:2757–3276.
6. Monteverde F, Bellosi A. The resistance to oxidation of an HfB_2–SiC composite. *J Eur Ceram Soc* 2005;**25**:1025–31.
7. Sciti D, Brach M, Bellosi A. Long-term oxidation behavior and mechanical strength degradation of a pressurelessly sintered ZrB_2–$MoSi_2$ ceramic. *Scr Mater* 2005;**53**:1297–302.
8. Clougherty EV, Hill RJ, Rhodes WH, Peters ET.*Research and Development of Refractory Oxidation-resistant Diborides, Part II, vol. II, Processing and Characterization*. 1970.
9. Coble RL, Hobbs HA. Sintering. In: Kauffman L, Clougherty EV, editors. *Investigation of Boride Compounds for very high Temperature Applications*. Springfield, VA: NTIS Report AD 428006, Federal Scientific and Technical Information; 1973. p. 82–100.
10. Jackson TA, Eklund DR, Fink AJ. High speed propulsion: performance advantage of advanced materials. *J Mater Sci* 2004;**39**: 5905–13.
11. Vanwie DM, Drewary Jr DG, King DE, Hudson CM. The hypersonic environment: required operating conditions and design challenges. *J Mater Sci* 2004;**39**:5915–24.
12. Loehman RE. Ultrahigh-temperature ceramics for hypersonic vehicle applications. *Ind Heat* 2004.
13. Opila E, Levine S, Lorincz J. Oxidation of ZrB_2- and HfB_2-based ultra-high temperature ceramics: effect of Ta additions. *J Mater Sci* 2004;**39**: 5969–77.
14. Fahrenholtz WG, Hilmas GE, Chamberlain AL, Zimmermann JW. Processing and characterization of ZrB_2-based ultra-high temperature monolithic and fibrous monolithic ceramics. *J Mater Sci* 2004;**39**: 5951–7.
15. Chamberlain A, Fahrenholtz W, Hilmas G, Ellerby D. Oxidation of ZrB_2–SiC ceramics under atmospheric and re-entry conditions. *Refract Appl Trans* 2005;**1**(2):1–8.
16. Rezaie AR, Fahrenholtz WG, Hilmas GE. Oxidation of zirconium diboride–silicon carbide at 1500 °C a low partial pressure of oxygen. *J Am Ceram Soc* 2006;**89**(10):3240–5.
17. Rezaie A, Fahrenholtz WG, Hilmas GE. Evolution of structure during the oxidation of zirconium diboride–silicon carbide in air up to 1500 °C. *J Eur Ceram Soc* 2007;**27**:2495–501.
18. Opeka MM, Talmy IG, Zaykoski JA. Oxidation-based materials selection for 2000 °C + hypersonic aerosurfaces: theoretical considerations and historical experience. *J Mater Sci* 2004;**39**:5887–904.
19. Wuchina E, Opeka M, Causey S, Buesking K, Spain J, Cull A, et al., Guitierrez-Mora F. Designing for ultrahigh-temperature applications: the mechanical and thermal properties of HfB_2, HfC_x, HfN_x and a-Hf(N). *J Mater Sci* 2004;**39**:5939–49.
20. Hu P, Wang G, Wang Z. Oxidation mechanism and resistance of ZrB_2–SiC composites. *Corros Sci* 2009;**51**:2724–32.
21. Li J, Lenosky TJ, Först CJ, Yip S. Thermochemical and mechanical stabilities of the oxide scale of ZrB_2 + SiC and oxygen transport mechanisms. *J Am Ceram Soc* 2008;**91**(5):1475–80.
22. Parthasarathy TA, Rapp RA, Opeka M, Kerans RJ. Effects of phase change and oxygen permeability in oxide scales on oxidation kinetics of ZrB_2 and HfB_2. *J Am Ceram Soc* 2009;**92**(5):1079–86.
23. Parthasarathy TA, Rapp RA, Opeka M, Kerans RJ. A model for oxidation of ZrB_2, HfB_2 and TiB_2. *Acta Mater* 2007;**55**:5999–6010.
24. Mitra R, Upender S, Mallik M, Chakraborty S, Ray KK. Mechanical, thermal, and oxidation behaviour of zirconium diboride based ultra-high temperature ceramic composites. *Key Eng Mater* 2009;**395**:55–68.
25. Zhang S, Li L, Kumar A. *Materials Characterization Techniques*. Boca Raton, FL: CRC Press; 2009. p. 267–93, Chap. 10.
26. Sandborg AO, Whitehead ME. Boron analysis and mapping with a windowless energy dispersive detector. *J Phys Colloques* 1984;**45**. C2:185–C2:188.
27. Thom AJ, Summers E, Mufit A. Oxidation behavior of extruded Mo5Si3Bx-MoSi2-MoB intermetallics from 600–1600 °C. *Intermetallics* 2002;**10**:555–70.
28. Cullity BD. *Elements of X-ray Diffraction*. New York, NY: Addison Wesley Publishing Company, Inc.; 1978. p. 447–78.
29. Schumann E, Sarioglu C, Blachere JR, Pettit FS, Meier GH. High temperature stress measurements during the oxidation of NiAl. *Oxid Met* 2000;**53**(3–4):259–72.

30. Paswan S, Mitra R, Roy SK. Oxidation behaviour of Mo–Si–B and Mo–Si–B–Al alloys. *Metall Mater Trans A* 2009;**40**:2644–58.
31. Alcock CB. The gaseous oxides of the platinum metals. *Platinum Met Rev* 1961;**5**(4):134–9.
32. Chase Jr MW. *NIST-JANAF Thermochemical Tables*. Fourth edition Woodbury, NY: J. Phy. Chem. Ref. Data, Monograph 9, American Institute for Physics; 1998.
33. Fahrenholtz WG. Thermodynamic analysis of ZrB_2–SiC oxidation: formation of a SiC-depleted region. *J Am Ceram Soc* 2007;**90**(1):143–8.
34. Antill JE, Warburton JB. Active to passive transition in the oxidation of SiC. *Corros Sci* 1971;**11**:337–42.
35. Narushima T, Goto T, Hirai T, Iguchi Y. High-temperature oxidation of silicon carbide and silicon nitride. *Mater Trans JIM* 1997;**38**(10):821–35.
36. Tripp WC, Davis HH, Graham HC. Effect of SiC addition on oxidation of ZrB_2. *Am Ceram Soc Bull* 1973;**52**:612–3.
37. Quanli J, Haijun Z, Suping L, Xiaolin J. Effect of particle size on oxidation of silicon carbide powders. *Ceram Int* 2007;**33**(2):309–13.
38. Lespade P, Richet N, Goursat P. Oxidation resistance of HfB_2–SiC composites for protection of carbon-based materials. *Acta Astronaut* 2007;**60**:858–64.
39. Brady MP, Gleeson B, Wright IG. Alloy design strategies for promoting protective oxide-scale formation. *JOM* 2000;**52**:16–21.
40. Paswan S, Mitra R, Roy SK. Oxidation behavior of the Mo–Si–B and Mo–Si–B–Al alloys in the temperature range of 700–1300 °C. *Intermetallics* 2007;**15**:1217–27.
41. Talmy IG, Zaykoski JA, Opeka MM, Dallek S. Oxidation of ZrB_2 ceramics modified with SiC and group IV–VI transition metal borides. In: McNallan M, Opila E, editors. *High Temperature Corrosion and Materials Chemistry III*. Pennington, NJ: The Electrochemical Society; 2001. p. 144–58.
42. Krishnamurty R, Srolovitz DJ. Stress distributions in growing oxide films. *Acta Mater* 2003;**51**(8):2171–90.
43. Chatterjee UK, Bose SK, Roy SK. Environmental degradation of metals. *Marcel Dekker* 2001:179–281.
44. Porter DL, Evans AG, Heuer AH. Transformation toughening in partially stabilized zirconia (PSZ). *Acta Metall* 1979;**27**:1649–54.
45. Wachtman JB. *Mechanical Properties of Ceramics*. New York: John Wiley & Sons; 1996.
46. Cutler RA. Engineering properties of borides. In: Schneider SJ, editor. *Ceramics and Glasses, Engineered Materials Handbook, Vol. 4*. Materials Park, OH: ASM International; 1992.